JOURNAL OF MATERIALS SCIENCE 15 (1980) 2435–2447

The effect of approach direction on damage in MgO due to spherical particle impact

D. G. RICKERBY, N. H. MACMILLAN
Materials Research Laboratory, Pennsylvania State University, University Park, PA 16802, USA

The damage produced by spherical particle impact against {100} surfaces of MgO has been investigated over a range of impact angles for a fixed particle velocity and over a range of particle velocities for a fixed impact angle. The mass of material removed by each impact was determined gravimetrically, and the crater and surrounding damage were studied by means of surface profilometry and scanning electron microscopy. A numerical computer model of the crater formation process was developed which was able to predict crater geometries in close agreement with those observed experimentally. This same model also provided estimates of the dynamic hardness, the contact time and the energy transmitted to the surface during the impact. The mean dynamic hardness was ~ 25% less than that measured in previous normal impact studies [1] on MgO of similar static hardness. The contact time and energy calculations give some insight into the reasons why the energy balance model, which successfully describes the velocity dependence of mass loss under normal impact conditions, breaks down for oblique impact.

1. Introduction

The present authors have previously reported [1] the results of single impact experiments in which spherical particles impinged at normal incidence against monocrystalline MgO surfaces of various crystallographic orientations. Both the volume of the crater produced and the mass of material removed from the surrounding region were found to be orientation dependent and proportional to the kinetic energy of the particle. In many situations of practical interest, however, erosion derives from solid particle impact at oblique as well as normal incidence, and it is therefore necessary to consider the effect of impact angle on erosive damage. Hence, the experiments described in the present paper extend the previous work by varying both the impact angle of the particle and the crystallographic direction of the component of the velocity vector parallel to the specimen surface.

Multiple impact experiments on ceramics and glasses [2–5] indicate that erosion increases as the impact angle increases from zero (grazing incidence), but generally passes through a maximum somewhat before the normal is reached. This maximum cannot be rationalized in terms of a simple energy balance model of the erosive process such as that proposed by Bitter [2]. It is therefore of interest to assess the influence on erosion of such additional factors as the contact time and frictional forces, which are not considered in this model. To this end a computer was used to calculate the particle trajectory during impact by an iterative numerical method.

2. Experimental procedure

Monocrystalline MgO specimens with {1 0 0} oriented target faces approximately 10 mm × 10 mm in size were cleaved from a large single crystal, chemically polished [6], and mounted in resin as in the previous work [1]. Table I shows the results of an emission spectroscopic analysis of the crystal, and indicates that both the total cation impurity content and the content of Fe plus Al lie within the range of variation found in the crystals used in the earlier work.

The particles used in the present experiments were WC–6 wt% Co spheres similar to those used

0022–2461/80/102435–13 $03.30/0

TABLE I Semi-quantitative spectrochemical analysis of the MgO crystal

Element	Concentration (ppm)
Ca	100
Al	20
Mn	30
Fe	200
Si	100

Not detected: Cr, Ti, V, Ni, Be, Cu, Ag, Na, Co, Zr, Cd, Zn, Sn, Bi, Ge, In, Ga, Pb, Sr, Ba.

previously. They were of nominal diameter 1.575 ± 0.025 mm, weighed 30 ± 1 mg, and had a Vickers hardness number (VHN) of approximately 2000 kg mm^{-2}. These particles were fired at the specimens by means of a nitrogen powered gas gun, and the particle velocities were determined to within $\pm$ 1% by means of a photoelectric time-of-flight device. The specimens were mounted on a goniometer stage which allowed the impact angle to be varied independently of the angle of rotation of the target surface about its normal.

In one series of experiments a study was made of the damage produced at an impact velocity of 200 ± 5 m sec^{-1} as the impact angle increased from 10° to 90°. Two sets of data were obtained, one with the particle velocity component parallel to the target surface along the ⟨1 0 0⟩ direction and the other with it parallel to the ⟨1 1 0⟩ direction. In another series of experiments the impact velocity was varied from 50 to 320 m sec^{-1} while the impact angle remained fixed at 30° to the surface. In this series the parallel component of the particle velocity was always along the ⟨1 0 0⟩ direction.

In some cases an indirect measurement of the velocity of the rebounding particle was made by arranging for it to impinge normally against the surface of an aluminium block. By measuring the depth of the crater thus produced it was possible to calculate the rebound velocity of the particle from the results of previous studies of crater formation in the same aluminium [7]. However, this technique was limited to those relatively small impact angles for which the aluminium block did not interfere with the flight of the particle between the gun muzzle and the MgO target.

The impact damage was characterized firstly by measuring gravimetrically the mass of material removed, and thereafter by examining the damaged region using scanning electron microscopy and surface profilometry. These last studies provided a series of parallel, equidistant cross-sectional profiles along the long axis of each crater. The crater volume could thus be determined by measuring the areas between the crater boundary and the original surface level for this series of profiles, and then applying the trapezoidal rule. In addition, crater depth relative to the same level was measured from that profile corresponding to the deepest cross-section through the crater.

Static indentation tests were also performed on the same chemically polished {1 0 0} MgO surfaces. The Meyer hardness M [8] was determined using a WC–6 wt% Co sphere of the type used in the impact experiments with an applied load of 50 kg, and the Meyer–Vickers hardness M_v* was determined using a standard Vickers diamond pyramid indenter with an applied load of 300 g. The measurements of indentation diameters or diagonals, as appropriate, were made along ⟨1 0 0⟩ directions in each case. Both of these hardness parameters are defined as the applied load divided by the *projected* area of contact, as is the dynamic hardness used in the impact model. The measured mean values of M and M_v and their standard deviations were 190 ± 20 kg mm^{-2} and 950 ± 20 kg mm^{-2}, respectively.

3. Theoretical

Being mathematically tractable, the normal impact problem has received a reasonable amount of attention [8, 9]. Consequently, only the pertinent results are given here. It is supposed that a rigid spherical particle of radius r and mass m impinges normally on a plastic–rigid half-space, and that the indentation pressure (dynamic hardness) p remains constant throughout the impact. If all the kinetic energy of the particle is assumed to be dissipated in plastic deformation of the target, then

$$pV = \tfrac{1}{2}mv_0^2, \tag{1}$$

where V is the crater volume and v_0 is the initial velocity of the particle. The contact time t_c is independent of the impact velocity, and is given by

$$t_c = \frac{\pi}{2}\left(\frac{m}{2\pi pr}\right)^{\frac{1}{2}}. \tag{2}$$

*M_v = (VHN) 0.927

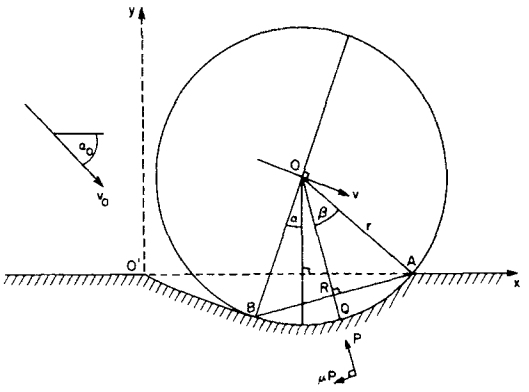

Figure 1 Schematic diagram of the oblique impact of a spherical particle against a half-space.

The oblique impact problem is more complicated because the equation of motion of the particle cannot be solved analytically. Hence, a computer program, details of which are discussed elsewhere [10], has been developed to provide a numerical solution by an iterative method. The approach used is similar to that adopted by Hutchings, Winter and Field [11], but incorporates a more accurate description of the area of contact [12, 13].

Fig. 1 illustrates the situation at some time long enough after the beginning of the impact that the sphere is no longer in contact with the entire surface of the crater. At this instant the particle velocity, which was initially v_0 at an angle α_0 to the x-axis, has reached a value v at an angle α, and the arc of contact in the x–y plane subtends an angle 2β at the centre of the sphere. It should be noted that, by convention, α is negative when the y-component of the particle velocity is directed into the surface. The principal retarding force P is taken to act along RO, and is assumed to derive from a constant, uniform indentation pressure acting over the projection of the area of contact onto the plane perpendicular to RO. In addition, a frictional force μP is taken to act tangentially through Q. As long as the sphere remains in contact with the entire surface of the crater, the

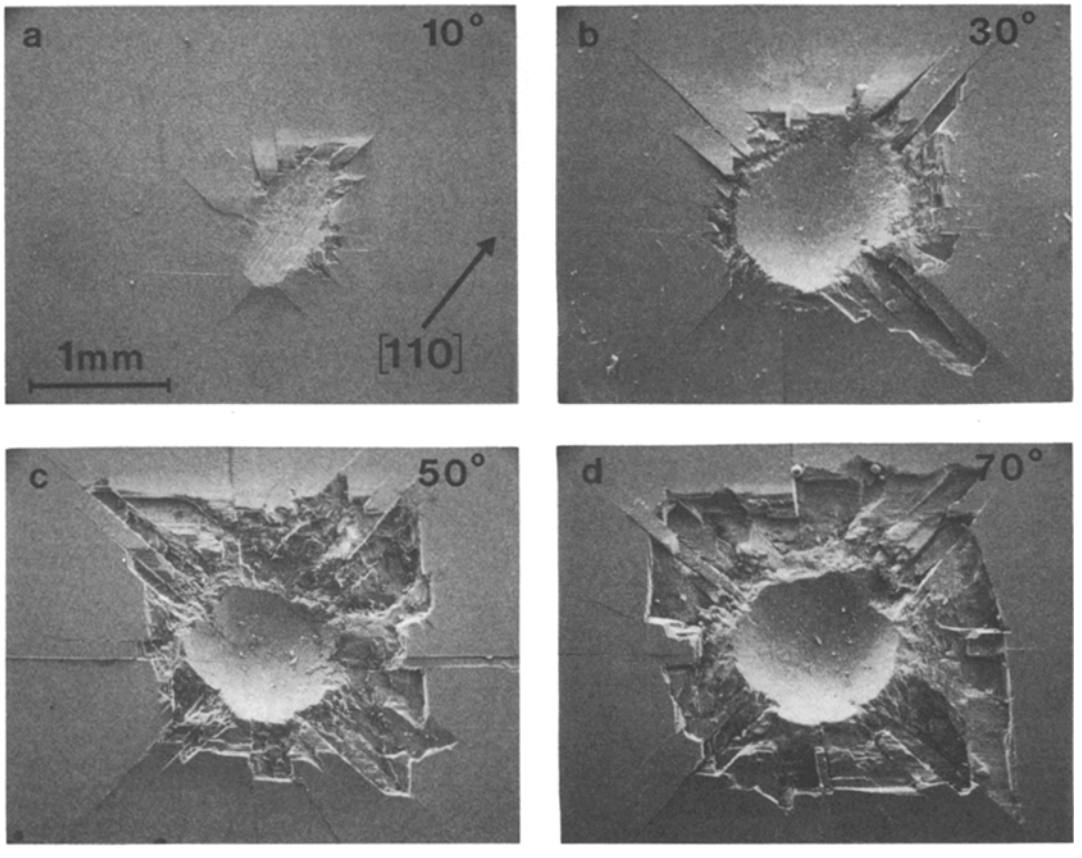

Figure 2 Scanning electron micrographs of craters formed along the ⟨1 0 0⟩ direction by 200 m sec^{-1} impacts at various angles.

motion can be described by

$$m\ddot{x} = -\mu P \quad (3)$$

and

$$m\ddot{y} = P. \quad (4)$$

However, once the sphere detaches from the surface at $0'$, the equations governing its translational motion become

$$m\ddot{x} = -P\sin(\alpha+\beta) - \mu P\cos(\alpha+\beta) \quad (5)$$

and

$$m\ddot{y} = P\cos(\alpha+\beta) - \mu P\sin(\alpha+\beta). \quad (6)$$

Each of these two pairs of equations can be solved numerically over that part of the motion to which it is applicable by means of an iterative procedure in which time is incremented in equal steps of appropriate duration. This procedure yields the complete particle trajectory, together with values of crater depth and volume, rebound velocity and rebound angle of the particle, and contact time.

4. Results

Fig. 2 shows the damage produced by 200 m sec^{-1} impacts in which the velocity component of the particle parallel to the target surface was directed along the ⟨1 0 0⟩ direction. Although its appearance varies considerably with impact angle, the damage consists, in general, of a crater formed mainly by plastic deformation, together with a peripheral region in which fracture occurs predominantly on {1 0 0} and {1 1 0} planes. As the impact angle is decreased, this latter region tends to concentrate increasingly around the exit side of the crater. Similar observations apply to the damage shown in Fig. 3, which was produced at the same impact velocity and angles, but with the parallel component of the particle velocity directed along the ⟨1 1 0⟩ direction. The effect of this change in approach direction on the appearance of the damage is most apparent at the smaller impact angles.

The series of micrographs shown in Fig. 4 illustrates the effect of varying the particle velocity while keeping the impact angle constant at 30°. At lower velocities the damage outside the crater is concentrated along the ⟨1 1 0⟩ directions on the exit side. As the velocity is increased, these regions

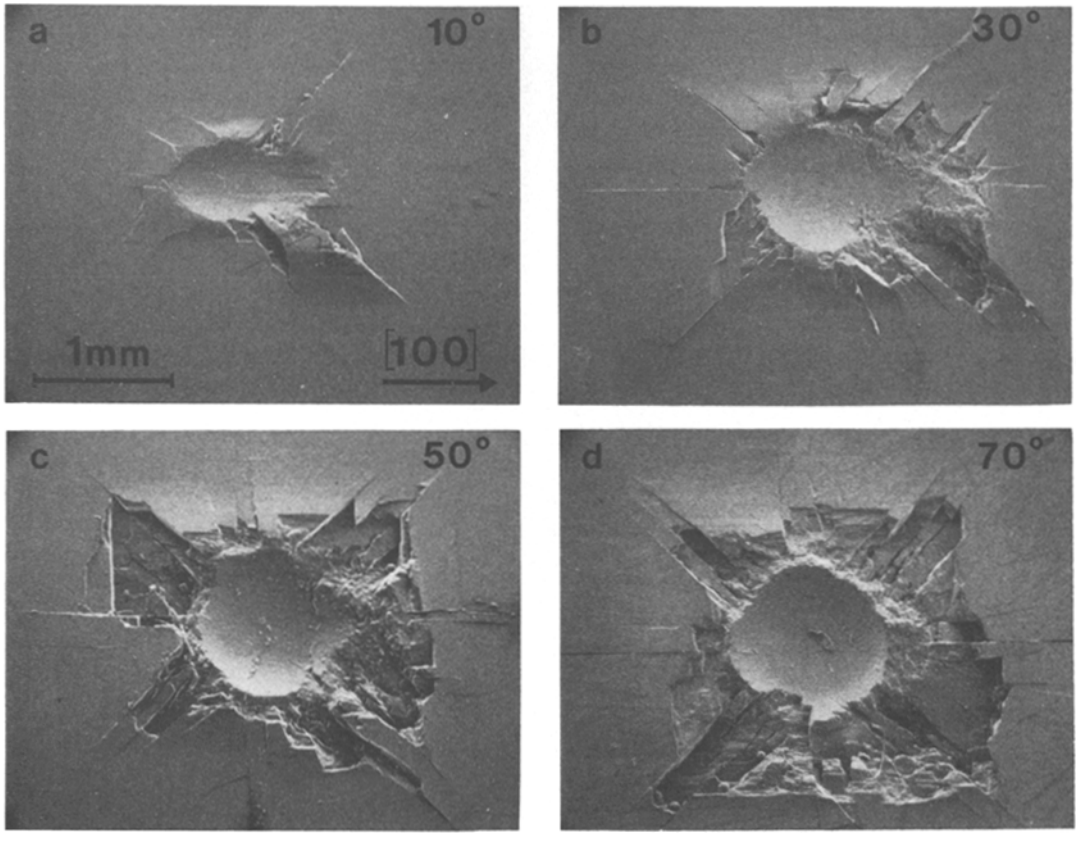

Figure 3 Scanning electron micrographs of craters formed along the ⟨1 1 0⟩ direction by 200 m sec^{-1} impacts at various angles.

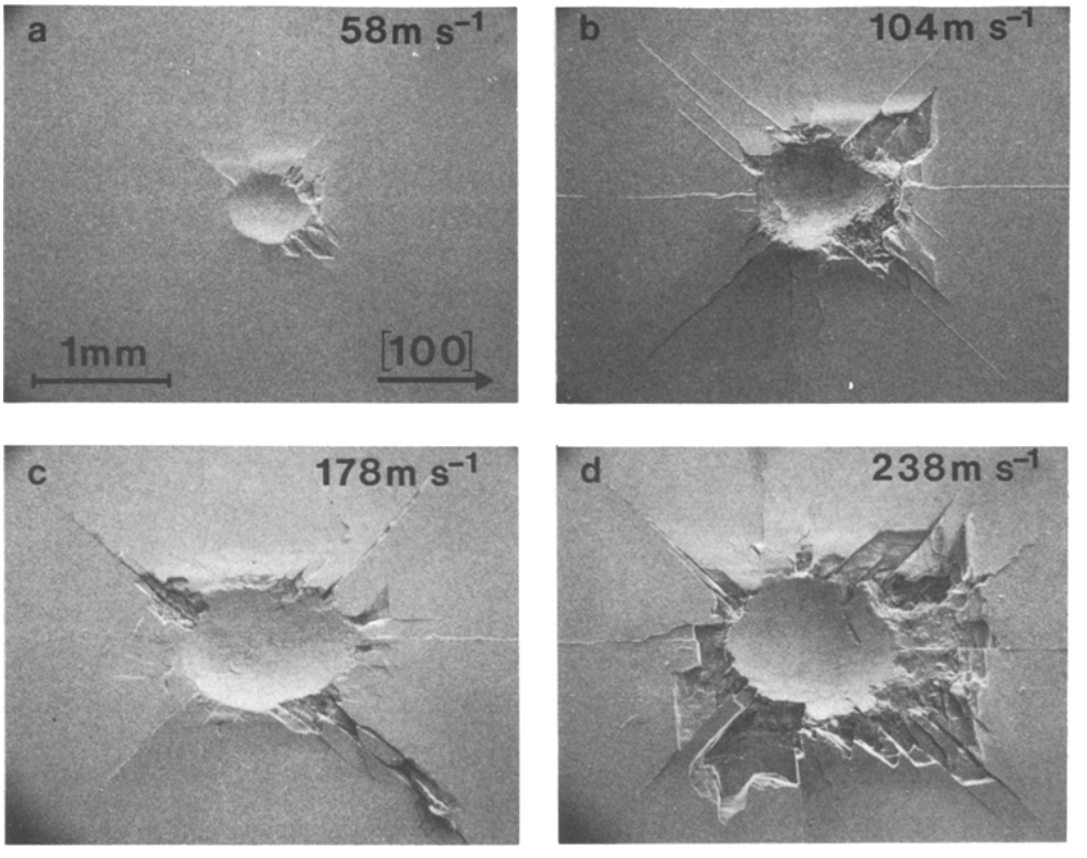

Figure 4 Scanning electron micrographs of craters formed along the ⟨1 0 0⟩ direction by different velocity impacts at 30° to the surface.

grow in size and are supplemented by smaller amounts of similar damage on the entrance side. Finally, at velocities above about 200 m sec^{-1}, the damaged regions begin to coalesce and to encroach back into the crater itself, resulting in significantly enhanced material removal.

Further details of the damage produced by impacts at an angle of 10° are shown in Fig. 5.* With the parallel component of particle velocity along the ⟨1 0 0⟩ direction, the slip lines around the crater all lie perpendicular to this direction, indicating that the deformation is produced by slip on tautozonal {1 1 0} planes inclined at 45° to it. However, when this velocity component lies along the ⟨1 1 0⟩ direction, two intersecting sets of slip lines are seen on each side of the crater. From the orientation of these lines, it can be deduced that the active {1 1 0} planes in this instance are inclined at 60° to the parallel velocity component and lie in two different zones. Fig. 5 also reveals that inside the craters there are networks of cracks lying predominantly perpendicular to the direction of the parallel velocity component. This cracking becomes less extensive as the impact angle increases towards 90° and, at any given impact angle, is usually more pronounced for a ⟨1 1 0⟩ orientation of the parallel velocity component than for a ⟨1 0 0⟩ orientation.

Near normal incidence any intersecting slip lines are generally confined, as in Fig. 6a, to narrow regions along ⟨1 1 0⟩ directions, and detailed examination of the eroded areas around the crater reveals complex patterns of cleavage steps on the fracture surfaces, such as those seen in Fig. 6b.

Nowhere in any of these micrographs is there any evidence of target melting during impact, and scanning electron microscopic studies of spent erosive particles revealed only insignificant amounts of MgO on their surfaces.

*The white debris on the surface was identified by energy dispersive X-ray analysis as WC.

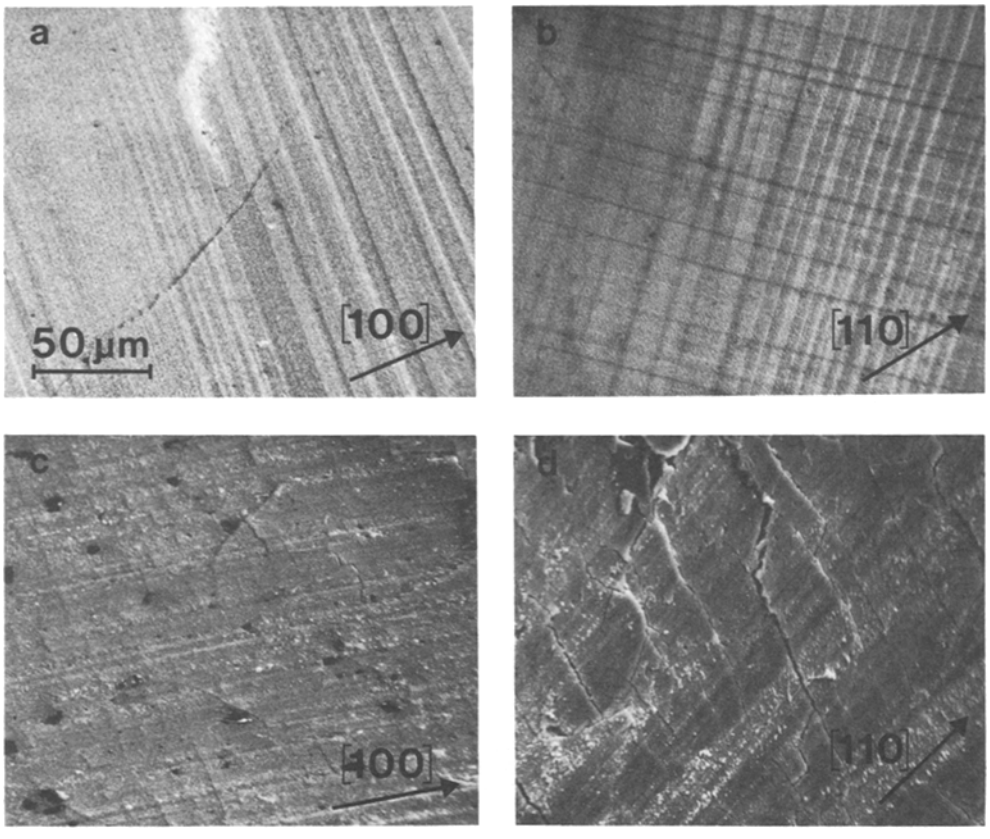

Figure 5 Detailed views of (a and b) slip outside the crater and (c and d) fracture inside produced by 10° impacts at 200 m sec^{-1}. The arrows indicate the direction of the component of particle velocity parallel to the surface.

The crater profiles shown in Figs. 7, 8 and 9 are cross-sections along the long axes of the craters of Figs. 2, 3 and 4, respectively. A comparison of Figs. 7 and 8 reveals that the crater shape does not differ greatly when the direction of the parallel component of particle velocity changes from ⟨1 0 0⟩ to ⟨1 1 0⟩. The broken lines superimposed on the profiles represent the crater shapes predicted theoretically, i.e. the envelopes of the successive positions of the circular boundary of the particle as generated by the computer program. Such discrepancies as exist presumably

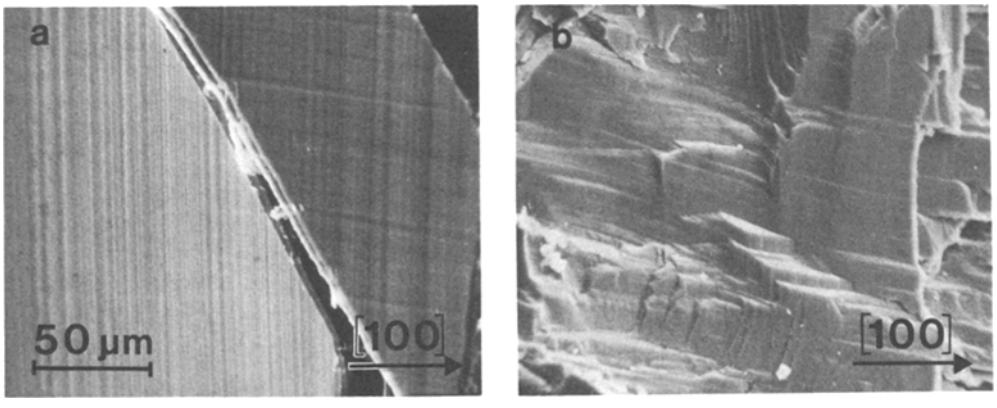

Figure 6 Details of (a) slip outside and (b) fracture in the eroded region around a crater made along the ⟨1 0 0⟩ direction by a 200 m sec^{-1} impact at 70° to the surface.

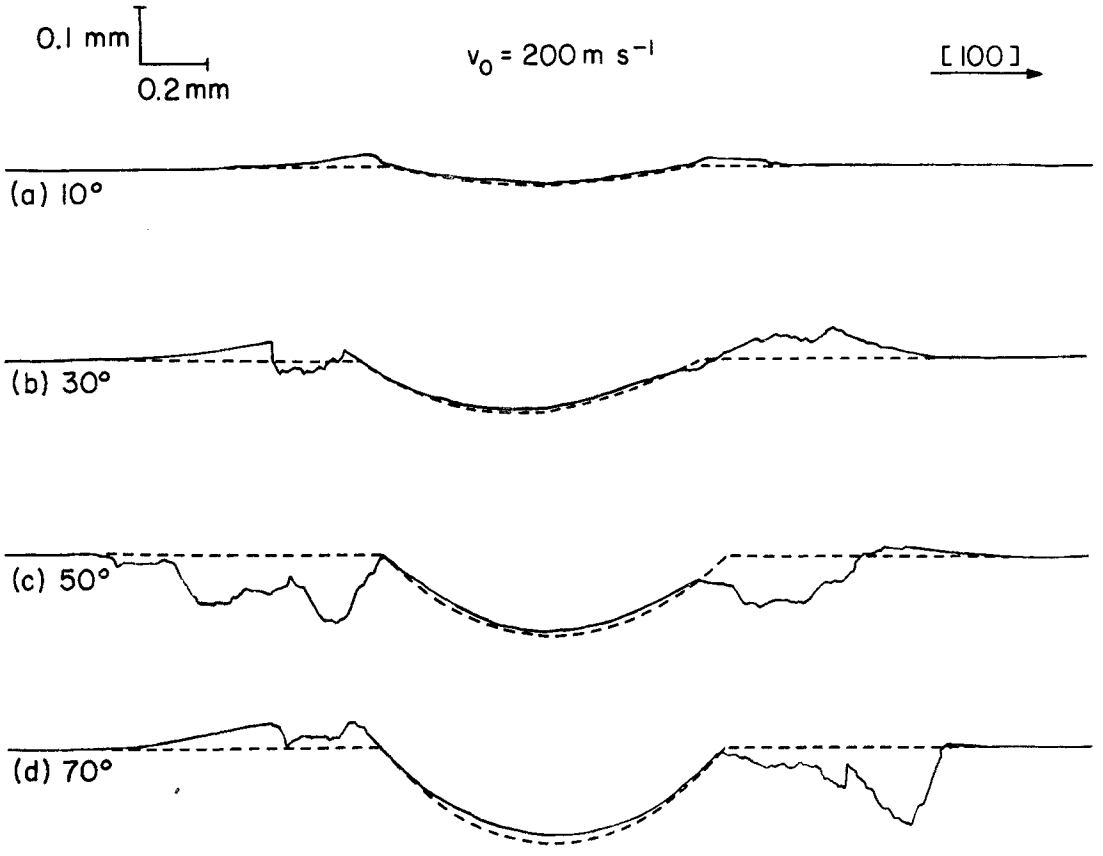

Figure 7 Profilometer traces along the axes of the craters shown in Fig. 2.

arise from experimental errors in the impact velocity and impact angle, and from the effect of elastic recovery of the target (which was not included in the theoretical model). The particles were hard enough that they did not undergo any appreciable plastic deformation during the impact, thereby eliminating this potential source of error.

The variation of crater volume with impact angle at an impact velocity of 200 m sec^{-1} is shown in Fig. 10, and the variation with velocity at an angle of 30° is shown in Fig. 11. The lines fitted to the experimental data correspond to the predictions of the computer model when p is taken as 780 kg mm^{-2}. This overall mean value of p, which has a standard deviation of 70 kg mm^{-2}, was obtained by making a first estimate from the volumes of the two normal impact craters, and then successively correcting this value until the discrepancies between the calculated and experimental crater volumes were minimized. The individual mean values of p for the three sets of volume data presented in Figs. 10 and 11 showed no significant deviation from the overall mean. The overall value was therefore used in all the final computations in this paper. A value of 0.1 was adopted for μ as being a reasonable estimate for a WC sphere sliding at high speeds on MgO [14, 15] in any crystallographic direction [16]. Varying μ between 0.5 and 0.2 affected the computed particle trajectories only marginally, so errors in μ within this range would not greatly alter the predictions of the model.

Measurements of crater depths were taken from the deepest profiles along each crater, and are shown in Figs. 12 and 13. The computer generated lines are a reasonable fit to the experimental data, confirming that no large discrepancies exist between the experimental and theoretical crater geometries. It is therefore concluded that neglecting plastic and frictional anisotropy and elastic recovery does not lead to any gross errors in the numerical calculations.

Mass loss as a function of impact angle at an impact velocity of 200 m sec^{-1} is shown in Fig. 14. The general trend is similar for both orientations of the parallel component of particle velocity: the

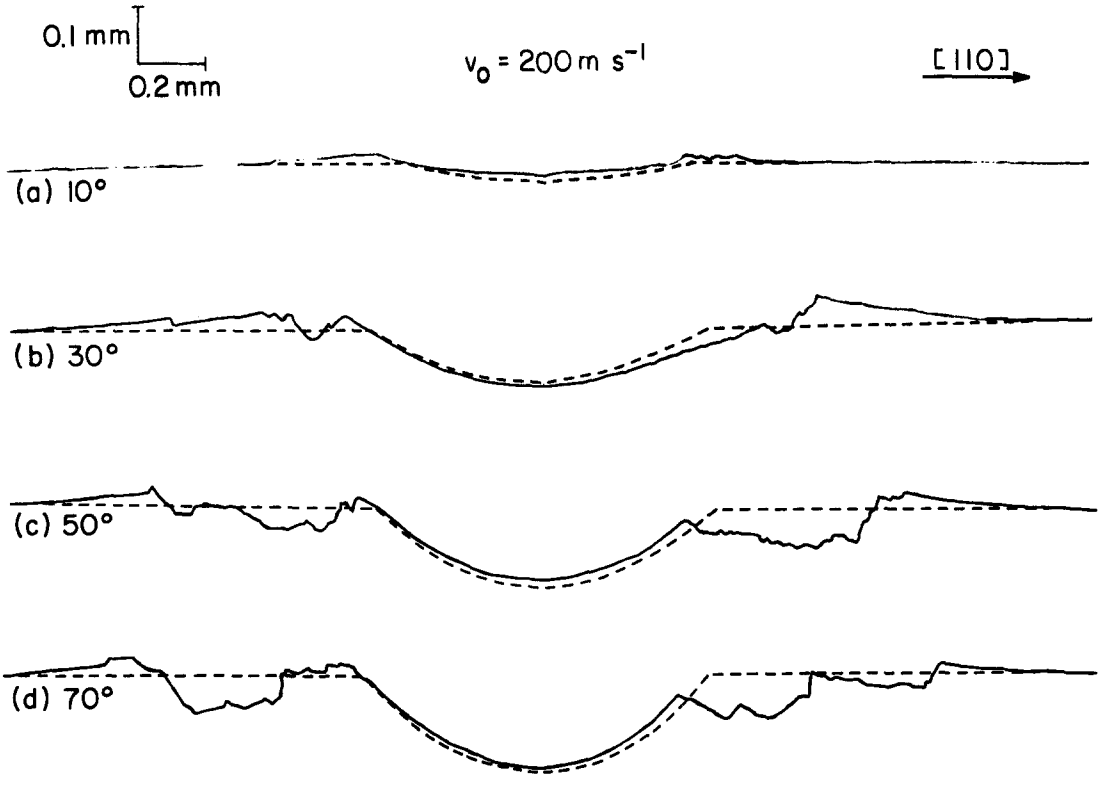

Figure 8 Profilometer traces along the axes of the craters shown in Fig. 3.

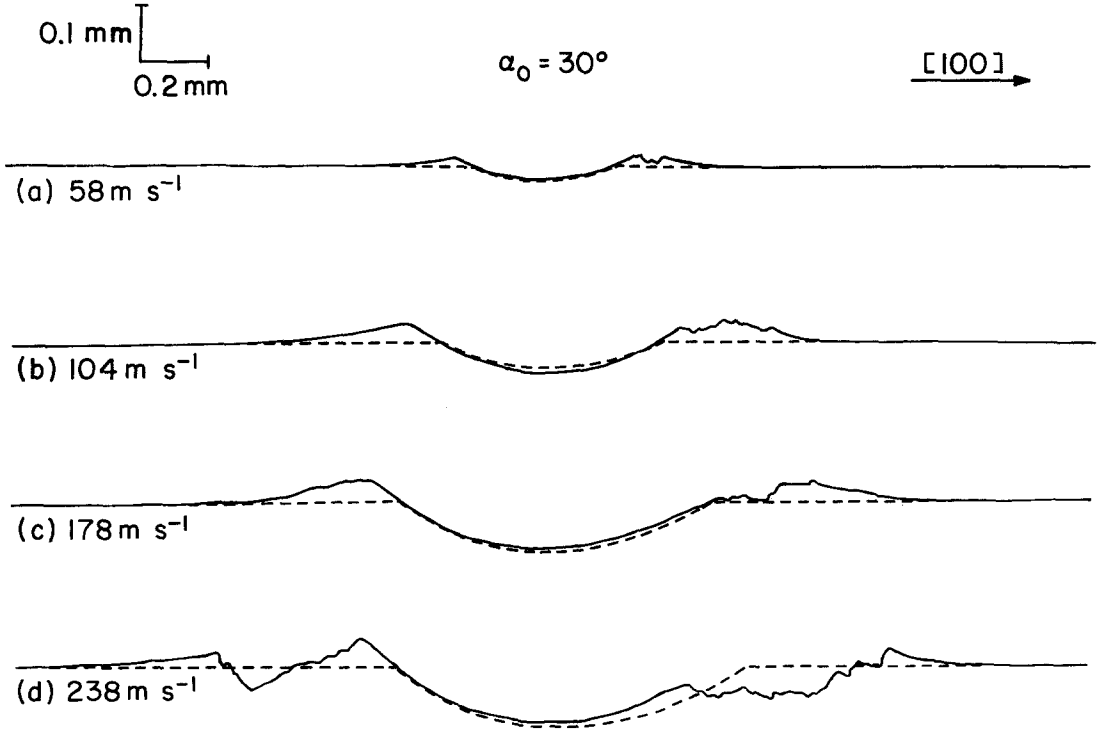

Figure 9 Profilometer traces along the axes of the craters shown in Fig. 4.

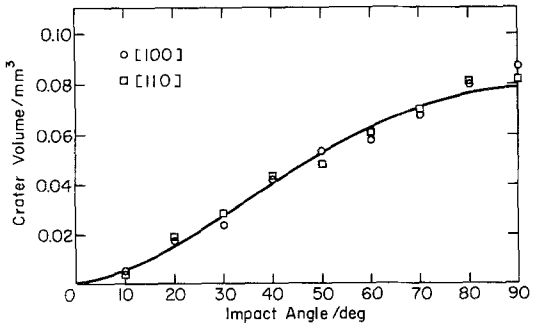

Figure 10 Variation of crater volume with impact angle at an impact velocity of 200 m sec^{-1}.

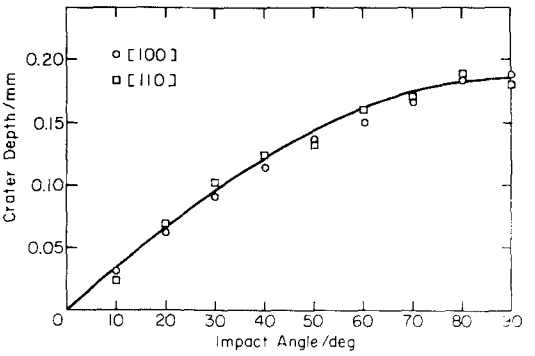

Figure 12 Variation of crater depth with impact angle at an impact velocity of 200 m sec^{-1}.

material removal increases monotonically with impact angle until a maximum is reached at about 80°, and then a slight decrease occurs as the angle approaches 90°. Similar maximum values occur in both cases, but the peak is somewhat sharper when the parallel component lies along the ⟨1 1 0⟩ direction rather than along the ⟨1 0 0⟩ direction. The two data points at 90° represent impacts performed under nominally identical conditions, and therefore give an indication of the variability of the experimental data. The variation of the mass loss with impact velocity at an impact angle of 30° is shown in Fig. 15. If a power function relationship between mass loss and impact velocity is assumed, the best fit to these data is obtained with a velocity exponent of 3.3. However, an exponential function of the velocity fits the complete data somewhat better, while a power function with a velocity exponent of 2.2 provides a reasonable fit to those data obtained at velocities below 220 m sec^{-1}.

Computer predictions of particle rebound velocities are shown in Figs. 16 and 17, together with the limited number of experimental data obtainable. These show that the agreement between theory and experiment is good for impacts at relatively small angles to the surface. Although no data are available for angles nearer the normal, it is likely that agreement would be less satisfactory in such cases because the rebound velocity would be more strongly affected by the elastic recovery of the target.

The energy transferred from the particle to the target during a single impact can easily be estimated from the computer model described in the previous section, since the total energy lost by the impinging particle is $\frac{1}{2}m(v_0^2 - v_R^2)$, where v_R is the particle rebound velocity. In this model particle rotation is neglected, and it is assumed that an amount pV of the energy transmitted to the target is used in plastic work, while the remainder is dissipated in overcoming frictional resistance. Both $\frac{1}{2}m(v_0^2 - v_R^2)$ and pV are plotted in Figs. 18 and 19 as functions of impact angle and velocity, respectively; and also shown is the parameter $\frac{1}{2}mv_0^2 \sin^2\alpha_0$, which corresponds to the transfer of energy to the target implied by Bitter's

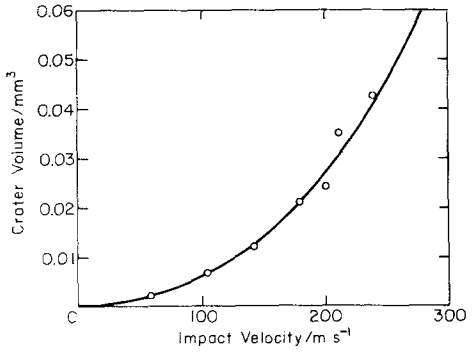

Figure 11 Variation of crater volume with impact velocity at an impact angle of 30°.

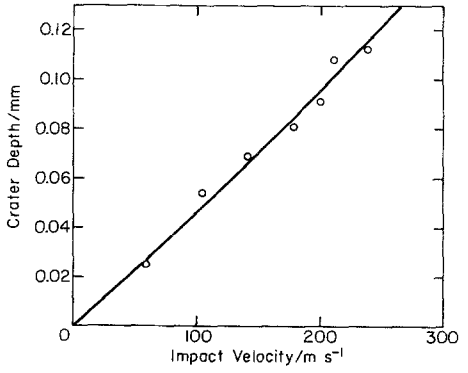

Figure 13 Variation of crater depth with impact velocity at an impact angle of 30°.

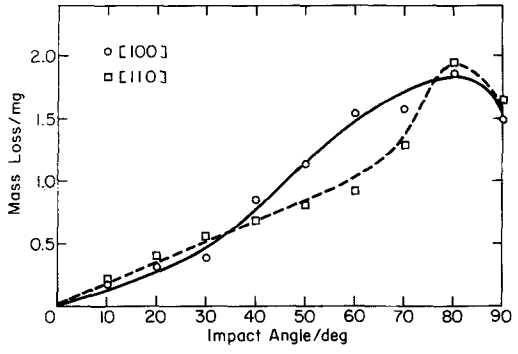

Figure 14 Mass loss as a function of impact angle at an impact velocity of 200 m sec^{-1}.

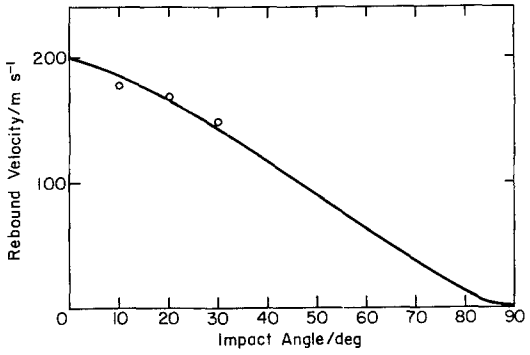

Figure 16 Rebound velocity as a function of impact angle at an impact velocity of 200 m sec^{-1}.

theory of erosion [2]. The parameters shown in Fig. 18 vary in a similar manner with impact angle, and the fraction of the total energy transferred which is dissipated as frictional work decreases markedly as the impact angle increases. Bitter's theory assumes that the energy transferred to the target during an impact is proportional to v_0^2, irrespective of the impact angle, while the computer model indicates that the parameters $\frac{1}{2}m(v_0^2 - v_R^2)$ and pV vary as $(v_0)^{2.20}$ and $(v_0)^{2.25}$, respectively, for an impact angle of 30°. The experimentally observed variation of mass loss with velocity at this angle is therefore consistent with the energy balance derived from the computer model, at least for impact velocities $\lesssim 200$ m sec^{-1}.

Finally, the computed values of the contact time t_c and the detachment time t_d at which the particle begins to separate from the surface of the crater are shown as functions of impact angle and impact velocity in Figs. 20 and 21, respectively.

The contact time decreases slowly with increasing impact angle up to about 60°, but then falls off rapidly as this angle approaches 90°. In contrast, it increases slowly with increasing impact velocity at an impact angle of 30°.

5. Discussion

The dynamic hardness data obtained from the present experiments not only have an overall mean value that is about 25% lower than that measured previously on a {1 0 0} surface [1], but also exhibit a two-fold reduction in their coefficient of variation. In addition, the amount of material removed by a single normal impact at 200 m sec^{-1} was about 40% less than in the previous experiments. These differences appear to be too large for them to be attributed merely to random scatter, but are difficult to explain unambiguously on the basis of the data presently available.

The reduction in the coefficient of variation probably reflects the fact that all of the specimens used in the present work came from the

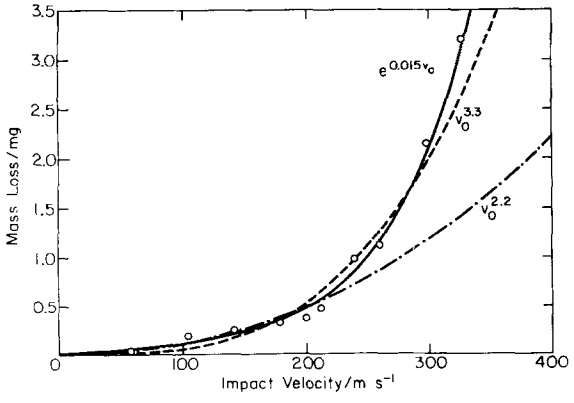

Figure 15 Mass loss as a function of impact velocity at an impact angle of 30°.

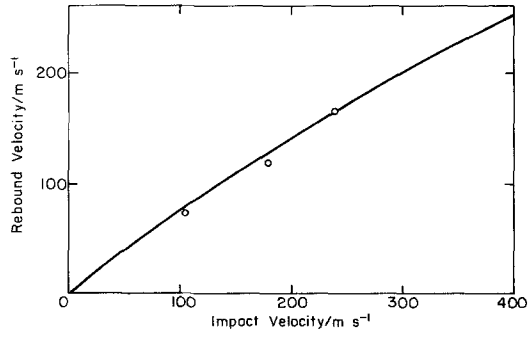

Figure 17 Rebound velocity as a function of impact velocity at an impact angle of 30°.

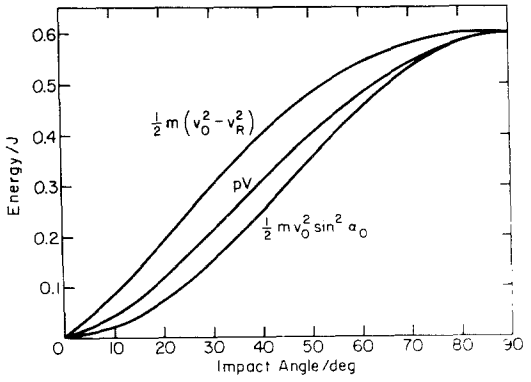

Figure 18 Comparison of different predictions of energy transfer as functions of impact angle at an impact velocity of 200 m sec^{-1}.

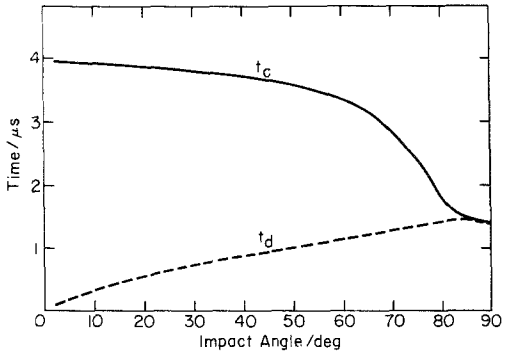

Figure 20 Contact and detachment times as functions of impact angle at an impact velocity of 200 m sec^{-1}.

same large monocrystal, and thus were of more consistent purity than the specimens used in the earlier work. It is also possible that the lower dynamic hardness and the reduction in the amount of material removed by fragmentation stem from a reduction in yield stress and/or work hardening and a concomitant increase in ductility, all of which derive from a lower total trivalent (Fe^{3+} plus Al^{3+}) cation impurity content [17–20] in the present specimens. However, the spectrochemical analyses performed on the different specimens lack both the capacity to distinguish between Fe^{2+} and Fe^{3+} ions and the sensitivity necessary to confirm this hypothesis. Furthermore, the corresponding reductions in the quasi-static Meyer and Meyer–Vickers hardnesses that should accompany any such reduction in impurity content were not observed, for the former did not change significantly and the latter decreased by only about 5%. This may indicate that quasi-static and dynamic hardness measurements are not strictly comparable, because they measure the stresses necessary to maintain very different numbers of dislocations in motion at very different average velocities; and there is evidence [21–23] that the stress required to maintain a given dislocation velocity varies more rapidly with Fe^{3+} content than does the yield stress [20].

In addition, it is important to recognize certain limitations of the methods used in both this work and the previous study to derive the dynamic hardness from the impact crater geometry. In both cases the separate contributions of such effects as work-hardening, plastic anisotropy, material pile-up ahead and to the sides of the impacting particle, stress-wave propagation and fracture are ignored. The net result of all these effects is interpreted in terms of a single parameter: the dynamic hardness. Consequently, changes in this parameter can only be directly related to changes in dislocation glide behaviour to the extent that this latter phenomenon dominates the process of crater formation. Unfortunately, the relative importance of dislocation glide in the present experiments is not clear.

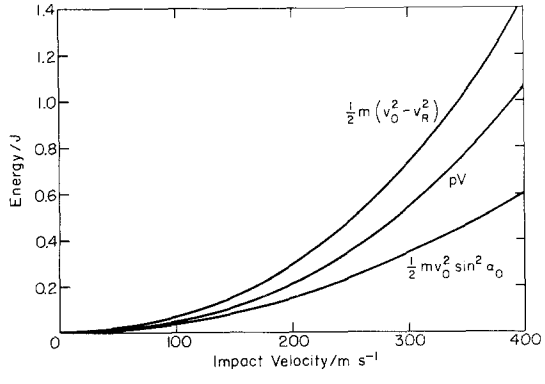

Figure 19 Comparison of different predictions of energy transfer as functions of impact velocity at an impact angle of 30°.

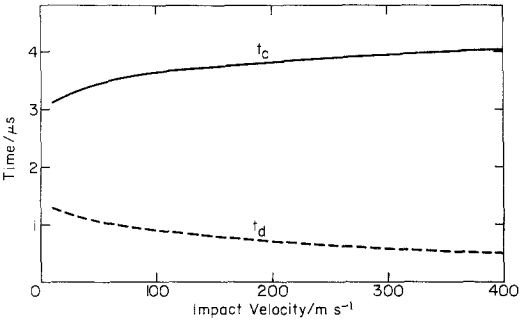

Figure 21 Contact and detachment times as functions of impact velocity at an impact angle of 30°.

It should also be realized that any change in the impact conditions has the effect of differently weighting the averaging process implicit in the derivation of the dynamic hardness. Thus, it is conceivable that an *apparent* difference in dynamic hardness could arise even in the absence of any change in dislocation glide behaviour, merely because the present value was obtained from a series of impacts made over a different range of velocities and angles from those in the previous experiments. This cannot be the full explanation, however, for the concomitant reduction in mass loss at normal incidence cannot be rationalized in the same fashion. It is therefore suggested that the observed differences arise, at least in part, from an increased sensitivity of hardness to impurity content at higher strain rates. If confirmed, this hypothesis might have important implications with respect to the erosion resistance of ceramic materials.

As far as can be ascertained from the present experiments, neither hardness anisotropy nor frictional anisotropy appear to exert a significant influence on crater shape. This was to be expected in the case of frictional anisotropy, which is low for blunt sliders [16]. However, it is rather more surprising that effects due to hardness anisotropy are not more evident when craters are formed along different crystallographic directions in the target surface, because the Knoop indentation hardness of a {1 0 0} MgO surface doubles as the long axis of the indenter rotates direction from ⟨1 0 0⟩ to ⟨1 1 0⟩ [24]. The differences between the slip line patterns produced around low angle impact craters along the ⟨1 0 0⟩ and ⟨1 1 0⟩ directions are due to slip occurring predominantly on two tautozonal slip planes in the former and on four planes in two different zones in the latter. Apparently, the combined effects of the different resolved shear stresses acting on the active slip planes in the two cases, the different dislocation–dislocation interactions occurring [25], and the different fracture processes initiated by these interactions [26], do not produce changes in crater geometry significantly greater than those arising from experimental error.

The simple assumption that the mass loss is proportional to the energy transmitted to the target during the impact is only partially successful in accounting for the observed variation of mass loss with impact angle. In particular, the maximum mass loss occurs at an angle near 80° rather than at normal incidence as expected theoretically. This appears to be associated with the predicted rapid increase in contact time that accompanies reduction of the impact angle from 90° to 70°, for such an increase would be expected to promote the formation of longer cracks in the damaged region around the crater and therefore to increase the amount of material removed from the surface. At smaller impact angles the contact time varies more slowly, and hence the experimental data conform more closely to the behaviour expected from an energy balance model. This result also suggests that any increase in stress wave interaction arising from a longer contact time has only a minor effect on material removal. Differences in the amount of material removed in impacts for which the parallel component of particle velocity lies along the ⟨1 0 0⟩ rather than ⟨1 1 0⟩ direction presumably reflect the different orientations of the non-radially symmetric stress field generated around the moving particle with respect to the dominant {1 0 0} and {1 1 0} cleavage planes. It is also interesting that the general form of the angular dependence of the mass loss arising from a single impact is similar to that found in multiple impact experiments [2–5].

For impacts at 30° to the surface, the energy balance model embodied in the computer program successfully accounts for the experimentally observed variation of mass loss with impact velocity, at least up to velocities in the region of 200 m sec^{-1}. At higher velocities, however, material removal tends to be increasingly greater than expected on the basis of this model. Thus, the velocity exponent obtained by fitting a power law curve to experimental mass loss data increases as the measurements are extended to higher impact velocities. The variation of the contact time with impact velocity does not appear to be sufficiently pronounced to account fully for this effect. Rather, it appears that the increased mass loss is associated with the removal of material from within the crater itself at velocities well below those at which this occurs for normal impact. This suggests that frictional traction is responsible for dragging material out of the crater. Such a mechanism would be expected to operate primarily at smaller impact angles, where the proportion of the available energy used in frictional work is greater.

It is thus apparent that even a theory based on the more precise energy balance derived from the

computer program cannot explain fully all the features of the erosion of materials which respond in a semi-brittle manner to particle impact. The replacement of the analytical approximations used previously by a more precise numerical calculation of the energy transferred to the target during the impact has resulted in some improvement in the correlation between theory and experiment. Those discrepancies which still remain appear to be qualitatively explicable in terms of the differences in contact times and frictional effects arising from variations in impact angle and particle velocity.

Acknowledgement

This work was supported by the U.S. Army Research Office under Contract No. DAAG29-79-C-0104.

References

1. D. G. RICKERBY, B. N. PRAMILA BAI and N. H. MACMILLAN, *J. Mater. Sci.* **14** (1979) 1807.
2. J. G. A. BITTER, *Wear* **6** (1963) 5.
3. G. L. SHELDON, *Trans. ASME: J. Basic Eng.* **92** (1970) 619.
4. C. E. SMELTZER, M. E. GULDEN and W. A. COMPTON, *Trans. ASME· J. Basic Eng.* **92** (1970) 639.
5. H. L. OH, K. P. L. OH, S. VAIDYANATHAN and I. FINNIE, "The Science of Ceramic Machining and Surface Finishing," edited by S. J. Schneider and R. W. Rice (NBS Special Publication 348, Washington DC, 1972) p. 119.
6. B. N. PRAMILA BAI and N. H. MACMILLAN, *J. Mater. Sci.* **14** (1979) 494.
7. D. G. RICKERBY and N. H. MACMILLAN, *Wear* **60** (1980) 369.
8. D. TABOR, "The Hardness of Metals" (Oxford University Press, London, 1951).
9. J. P. ANDREWS, *Phil. Mag.* **9** (1930) 593.
10. D. G. RICKERBY and N. H. MACMILLAN, *Int. J. Mech. Sci.*, to be published.
11. I. M. HUTCHINGS, R. E. WINTER and J. E. FIELD, *Proc. Roy. Soc.* **A348** (1976) 379.
12. G. BIRKHOFF, G. D. BIRKHOFF, W. E. BLEICK, E. H. HANDLER, F. D. MURNAGHAN and T. L. SMITH, "Ricochet off Water," (AMP Memo. 42.4M 1944).
13. W. JOHNSON and S. R. REID, *J. Mech. Eng. Sci.* **17** (1975) 71.
14. F. P. BOWDEN and P. A. PERSSON, *Proc. Roy. Soc.* **A260** (1961) 433.
15. D. R. MILLER, *ibid.* **A269** (1962) 368.
16. F. P. BOWDEN and C. A. BROOKES, *ibid.* **A295** (1966) 244.
17. G. W. GROVES and M. E. FINE, *J. Appl. Phys.* **35** (1964) 3587.
18. M. SRINIVASAN and T. G. STOEBE, *J. Appl. Phys.* **41** (1970) 3726.
19. R. W. DAVIDGE, *J. Mater. Sci.* **2** (1967) 339.
20. C. N. AHLQUIST, *J. Appl. Phys.* **46** (1975) 14.
21. R. N. SINGH and R. L. COBLE, *ibid.* **45** (1974) 981.
22. *Idem, ibid.* **45** (1974) 990.
23. *Idem, ibid.* **45** (1974) 5129.
24. C. A. BROOKES, J. B. O'NEILL and B. A. W. REDFERN, *Proc. Roy. Soc.* **A322** (1971) 73.
25. B. H. KEAR, A. TAYLOR and P. L. PRATT, *Phil. Mag.* **5** (1959) 665.
26. Y. T. CHOU and R. W. WHITMORE, *J. Appl. Phys.* **32** (1961) 1920.

Received 21 January and accepted 21 February 1980.